Surface structural conversion and electrochemical enhancement by heat treatment of chemical pre-delithiation processed lithium-rich layered cathode material

Shaojie Han [a, b], Bao Qiu [a], Zhen Wei [a], Yonggao Xia [a, *], Zhaoping Liu [a, *]

[a] Ningbo Institute of Materials Technology and Engineering, Chinese Academy of Sciences, Zhejiang 315201, PR China
[b] The School of Material Science and Chemical Engineering, Ningbo University, Zhejiang 315211, PR China

HIGHLIGHTS

- The surface structure transforms from layered to spinel during heat treatment.
- The surface spinel undergoes an internal structural evolution at high temperature.
- The electrochemical performances are obviously improved after heat treatment.
- The mechanism of structural transformation is discussed.

GRAPHICAL ABSTRACT
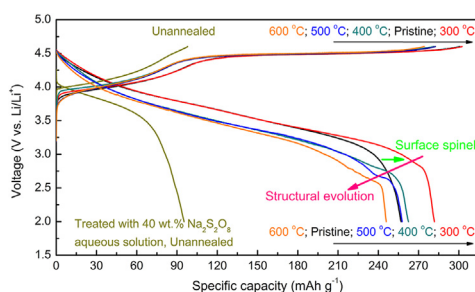
ARTICLE INFO

ABSTRACT

A surface modification strategy through soaking in $Na_2S_2O_8$ aqueous solution and then annealing has been developed for Li-rich layered cathode materials for Li-ion batteries. The modified materials have a significant improvement on electrochemical performances. The initial discharge capacity increases from 257 to 285 mAh g^{-1}, and the initial coulombic efficiency increases from 85.4% to 93.2% in the voltage rang of 2.0–4.6 V. The electrochemical enhancement mechanism has been revealed by detailed investigations on the surface structural conversion of the material. X-ray photoelectron spectroscopy (XPS) and inductively coupled plasma-atomic emission spectrometry (ICP) confirm that $Na_2S_2O_8$ oxidizes lattice oxygen to formal O_2^{2-} species and the corresponding Li$^+$ is extracted from the material surface. On the subsequent annealing, the formal O_2^{2-} species turn to O_2 and release from the particle surface. The increased oxygen vacancies induce structural rearrangement and lead to the phase transition from layered ($R\text{-}3m$ or $C2/m$) to spinel ($Fd3m$) at the particle surface, which is supported by X-Ray Diffraction (XRD) and high resolution transmission electron microscope (HRTEM). It is also found that the spinel phase increases with the increasing annealing temperature, and an internal structural evolution from LiM_2O_4-type spinel to M_3O_4-type spinel takes place at the same time.

© 2014 Elsevier B.V. All rights reserved.

1. Introduction

Rechargeable lithium-ion batteries (LIBs) have served as power-sources for portable electronics for many years [1–3]. With *Tesla Motors, Inc.* (a company that designs, manufactures and sells electric cars and electric vehicle powertrain components) launched

* Corresponding authors. Tel./fax: +86 574 8668 5096.
  E-mail addresses: xiayg@nimte.ac.cn (Y. Xia), liuzp@nimte.ac.cn (Z. Liu).

popular electromobile *Model S*, it seemed that the spring time for LIBs to expand their application to power-sources for electric vehicles (EVs) was coming. However, lake of high performance cathode materials is still a technological bottleneck for the commercial development of advanced LIBs [4,5]. The current commercial LIBs cathode materials contain layered transition metal oxides, $LiTMO_2$ (TM = Mn, Ni, Co and their combination); Mn based spinels ($LiMn_2O_4$) and olivine-type lithium iron phosphate ($LiFePO_4$) [6—10]. The nominal capacity of these cathode materials are limited below 200 mAh g^{-1}, which cannot meet the requirement of high energy-density in EV applications [11]. Therefore, there is an urgent need to develop the next generation of high performance LIBs cathode material.

The Li-rich layered oxides, structurally described as 'layered—layered' $xLi_2MnO_3 \cdot (1 - x)LiTMO_2$ (TM = Mn, Ni, Co, etc.), can deliver reversible capacities exceeding 250 mAh g^{-1} with the average operating voltage of about 3.5 V (vs. Li/Li$^+$) [12—19]. Among all the reported cathode materials, they seem to be the most prospective candidate and have attracted worldwide interest in the past few years. A characteristic feature of the Li-rich layered oxides is a voltage plateau at ~4.5 V during the initial charge, which corresponds to the activation of Li_2MnO_3 and is considered to be the origin of their extra high capacities [17,20,21]. However, this activation process causes an irreversible structural rearrangement in the material bulk and the release of O_2 from the particle surface region, which lead to a large capacity loss (40—100 mAh g^{-1}) in the following discharge. The low initial coulombic efficiency is just one of the barriers for their practical application in Li-ion batteries. The other weaknesses include their poor rate performance and cycling stability, may be also resulting from the release of O_2 which damages the surface structure of the materials [22].

Therefore, the key to overcoming the above issues is to stabilize the surface structure of these materials. Surface modification is considered to be one of the most promising approaches. Coating Li-rich layered oxides with metal oxides, phosphates or fluorides like Al_2O_3, ZnO, $AlPO_4$, $CoPO_4$, AlF_3 etc., have been shown to effectively improve the electrochemical performances of these materials [23—29]. The coating layers are always thought to be responsible for the retention of part of the oxygen vacancies in the lattice after the initial charge, as well as the suppression of undesired solid electrolyte interface (SEI) layers and the fast charge transfer reaction kinetics. Recently, a growing body of research employs spinel materials for surface modification of Li-rich layered oxides. F. Wu et al. [30] reported a reasonable design and synthesis of spinel/layered heterostructured material, by encapsulating a layered Li-rich material with a nanospinel mixture $LiNi_xMn_{2-x}O_4$ ($0 \leq x \leq 0.5$). Because of high Li$^+$ ionic and electronic conductivity of the spinel $LiNi_xMn_{2-x}O_4$, the discharge capacity of the material was immensely improved. B. Song et al. [31] mixed Li-rich layered oxides with Super P (carbon black) and transformed the layered phase of Li_2MnO_3 to spinel-like phase at the surface region of particles during post annealing process at 350 °C. Both the initial coulombic efficiency and the rate capability were significantly increased. J. Zhen et al. [32] blended Li-rich layered oxides in $Na_2S_2O_8$ or $(NH_4)_2S_2O_8$ solution and then fully dried. The initial coulombic efficiency and the rate capability were also improved obviously. They claimed that the enhanced electrochemical performances were benefited by the formation of surface spinel-like phase, although they did not expound the formation mechanism. In a word, the above researches suggest that surface modification with spinel structure is of great potential to obtain high-power Li-rich layered oxides for Li-ion batteries.

The objective of this work is to transform the surface structure of the as-prepared Li-rich layered oxide $Li_{1.143}Mn_{0.544}Ni_{0.136}Co_{0.136}O_2$ from layered to spinel through a method of surface

modification. Benefited by the generated spinel layer, the initial coulombic efficiency, initial discharge capability and rate capability of the modified materials have been significantly improved as desired. Here, $Na_2S_2O_8$ aqueous solution was introduced to extract Li$^+$ from the surface region of the Li-rich layered oxide, and its reaction mechanism was detailed studied. Moreover, the subsequent annealing treatment is reasonably believed to be responsible for spinel formation at the material surface based on comprehensive analysis of the results of HRTEM, SEM, XRD, XPS and electrochemical characterizations.

2. Experimental

2.1. Material preparation and treatment

Layered $Li_{1.143}Mn_{0.544}Ni_{0.136}Co_{0.136}O_2$ was synthesized using spherical $(Mn_{4/6}Ni_{1/6}Co_{1/6})CO_3$ precursor. The precursors were prepared through a coprecipitation method from Mn, Ni, Co sulphate salt solution with a desired stoichiometric ratio and Na_2CO_3 aqueous solution. Then the obtained spherical $(Mn_{4/6}Ni_{1/6}Co_{1/6})CO_3$ precursor were mixed with proper amounts of Li_2CO_3. Finally, the resultant mixture was heated in air at 500 °C for 5 h followed by heating at 850 °C for 10 h.

The different weights of $Na_2S_2O_8$ (3 g, 4 g and 5 g) were first dissolved in 200 ml deionized water. Then the lithium rich material powders (10 g) were introduced into different concentrations of $Na_2S_2O_8$ solutions under stirring. The obtained mixtures were maintained under stirring for 24 h. Afterwards, the powders of the three samples were filtered, washed thoroughly with deionized water and dried in an oven at 80 °C. Finally, the de-lithiated powders were heated at 300, 400, 500 or 600 °C for 10 h with the heating rate of 5 °C min^{-1} in air, respectively.

2.2. Characterization

The crystal structure of the materials was confirmed by X-ray Diffractometer (D8 Advance, Bruker AXS) using Cu-Kα radiation source ($\lambda_1 = 1.54056$ Å, $\lambda_2 = 1.54439$ Å) with a scan rate of 0.4° min^{-1} between 5 and 135° 2θ. High-resolution TEM images were obtained using an S-Twin electron microscopy (FEI Tecnai F20) operating at 200 kV. Particle morphologies were revealed by a scanning electron microscope (Fe-SEM) (S-4800 Hitachi, 15 kV). XPS measurements were carried out with an X-ray photoelectron spectrometer (Kratos AXIS Ultra DLD), using a focused monochromatized Al K$_\alpha$ radiation (1486.6 eV). All binding energies are referenced with respect to the aliphatic carbon signal (C_{1s}) to 284.8 eV. Li, Co, Ni and Mn contents include in the materials were determined using an inductively coupled plasma-atomic emission spectrometry (ICP, Optima 2100) after the complete dissolution of the powders into an acidic solution.

2.3. Electrochemical measurement

All the electrochemical cycling tests were conducted using CR2032-type coin cell with lithium metal as negative electrodes. Composite positive electrodes consisted of 80 wt.% active material, 10 wt.% Super P, and 10 wt.% polyvinylidene fluoride (PVdF) binder in NMP, pasted on an aluminium foil as a current collector. They were then pressed at 8 MPa after drying at 80 °C overnight. The electrolyte solution used was 1 M LiPF$_6$ dissolved in a mixture of ethylene carbonate (EC) and dimethylcarbonate (DMC) 3:7 in volume (Guotai-Huarong New Chemical Material Co., Ltd). The cells were assembled in an argon filled glovebox. The galvanostatic charge—discharge tests were carried out from a LAND battery program-control test system (Wuhan, China) between 2.0 and 4.6 V

Table 1
Chemical compositions determined by ICP for the pristine sample as well as N-30, N-40 and N-50 samples.

Sample	Li	Mn	Co	Ni
Pristine	1.15	0.547	0.135	0.134
30 wt.% $Na_2S_2O_8$ (N-30)	1.10	0.550	0.133	0.133
40 wt.% $Na_2S_2O_8$ (N-40)	1.10	0.548	0.134	0.134
50 wt.% $Na_2S_2O_8$ (N-50)	1.08	0.548	0.134	0.134

at the charge–discharge rates from 0.1 to 1 C at room temperature. Electrochemical impedance spectroscopy (EIS) measurement was performed on an Autolab modular electrochemical system (Autolab PGSTAT302N) over a frequency range of 100 kHz to 0.01 Hz at the first time charging state of 4.6 V.

3. Results and discussion

Li, Mn, Co and Ni contents of the materials were determined by ICP (from the ratios of the amounts of Li, Mn, Co and Ni and fixing the total amount of transition metal ions to 0.816). Herein, according to the different weight ratios applied to treat $Li_{1.143}Mn_{0.544}Ni_{0.136}Co_{0.136}O_2$, 30 wt.%, 40 wt.% and 50 wt.% $Na_2S_2O_8$ treated samples are designated as N-30, N-40 and N-50, respectively. The analytical results are shown in Table 1. It is found that the chemical formula of the prepared pristine samples is very close to the ideal $Li_{1.143}Mn_{0.544}Ni_{0.136}Co_{0.136}O_2$ chemical stoichiometry, although the experimental Li ratio is a little greater than the theoretical composition. Comparing the data of all the samples, it is confirmed that Li has been extracted from the material after being treated with $Na_2S_2O_8$ aqueous solution, and the amount increases with the increasing concentration of $Na_2S_2O_8$.

HRTEM was employed to detect the structural changes of the samples before and after treatment. In Fig. 1a, obvious morphological differences are observed between the pristine sample and N-40 sample. Typical layered (003) rhombohedral and (001) monoclinic lattice fringes are presented in the pristine sample, which are straight and continue to the surface of particle. By contrast, the structural regularity of N-40 sample is damaged at the particle surface, as shown in Fig. 1b. It indicates that the reaction between $Na_2S_2O_8$ and active material is very fierce. Undoubtedly, this structural damage will increase the transmission resistance of lithium ions during electrochemical cycling, and lead to a large degradation of the electrochemical properties. Nevertheless, this kind of damage seems to be slight on the level of the whole particle. Fig. 1c and d shows the SEM images of the pristine sample and the N-40 sample. The morphologies of the particles do not change obviously after the treatment with the $Na_2S_2O_8$ aqueous solution.

Fig. 2a shows the first charge/discharge curves during electrochemical cycling of the corresponding samples. They were tested versus Li in coin cells cycling between 2.0 and 4.6 V at 0.1 C (1 C = 250 mA g^{-1}). The pristine sample shows a representative profile of Li-rich layered cathode materials, including a sloping curve below 4.5 V and a plateau around 4.5 V in charge and continuous sloping curve in discharge. For N-40 sample, however, the plateau around 4.5 V disappears and the discharge capacity decays to less than 100 mAh g^{-1}. It suggests that after being treated with $Na_2S_2O_8$ aqueous solution, the Li_2MnO_3 in the material cannot be activated below 4.6 V during the initial charge (In fact, it can be activated slowly in the following cycles, as shown in Supplementary Fig. S1). When we increase the cut-off voltage to 4.8 V and reduce the charging rate to 0.05 C, the voltage plateau appears again, but increases to around 4.6 V. But the discharge
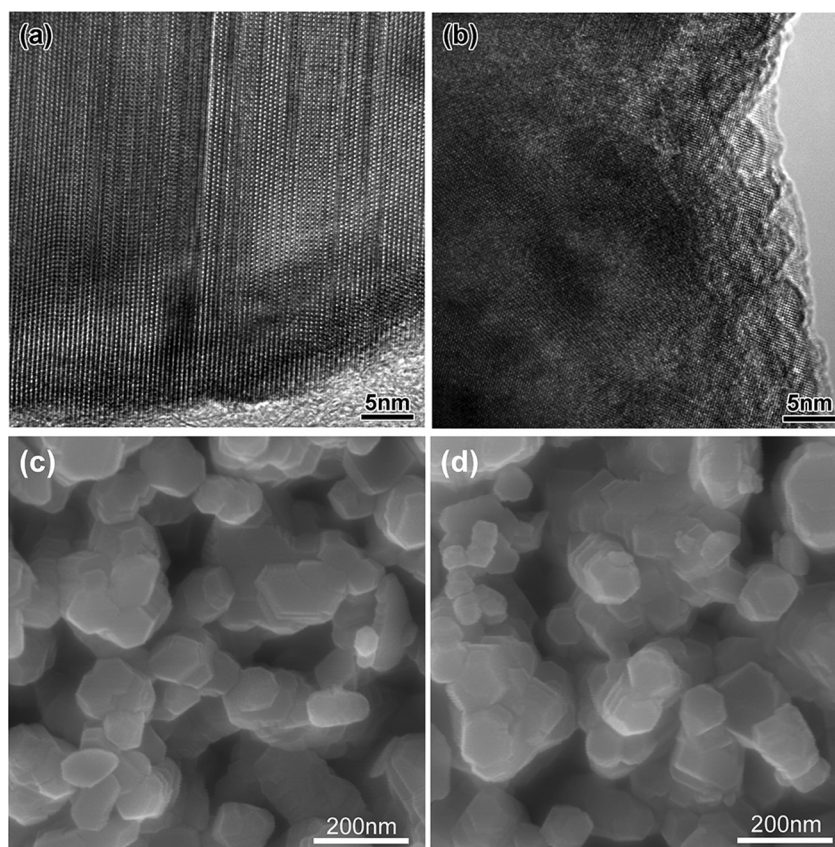

Fig. 1. HRTEM images of (a) the pristine sample, (b) the N-40 sample. SEM images of (c) the pristine sample, (d) the N-40 sample.
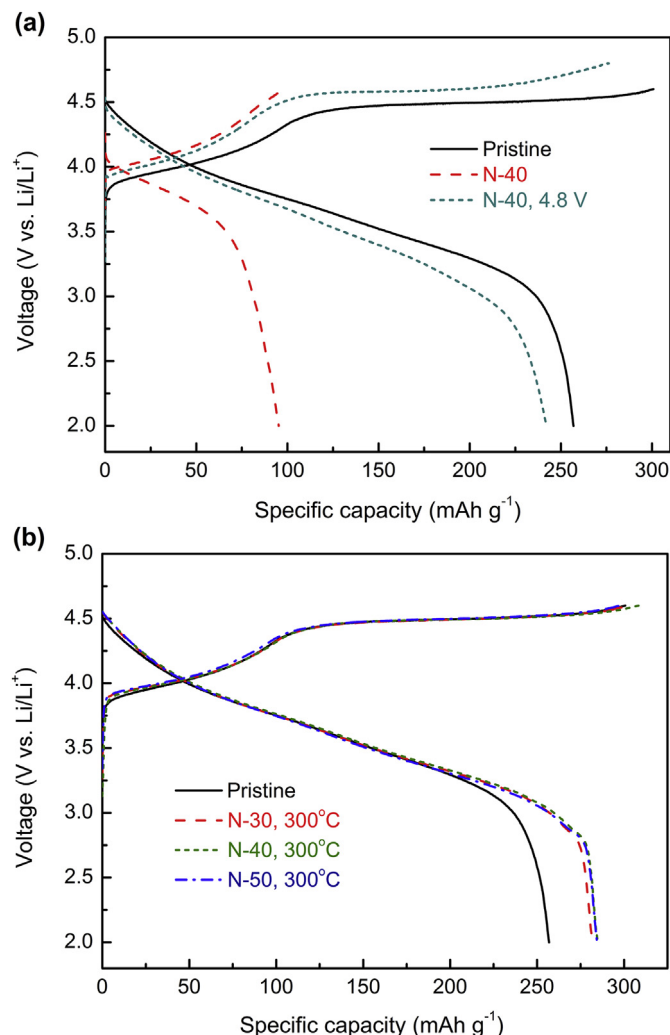
Fig. 2. Initial charge/discharge profiles of (a) the pristine sample and N–40 sample; (b) the pristine sample and the N–30, N–40 and N–50 samples annealed at 300 °C. All the half batteries were cycled between 2.0 and 4.6 V at 0.1 C, except one of N–40 samples in (a) which was cycled between 2.0 and 4.8 V at 0.05 C.

28 wt.% (N-28), 40 wt.% (N-40), 49 wt.% (N-49), 60 wt.% (N-60) and 76 wt.% (N-76) $Na_2S_2O_8$ when cycled between 2.0 and 4.8 V at 0.1C. There is a linear relationship between the initial coulombic efficiency and the concentration of $Na_2S_2O_8$, which confirms that the initial coulombic efficiency of the material can be controlled by simply adjusting the dosage of $Na_2S_2O_8$. However, it should be noted that higher initial coulombic efficiency is not equal to higher discharge capacity, as demonstrated by the data of N-40 and N-50 samples. Among the three samples, the N-40 achieves the highest initial discharge capacity and acceptable initial coulombic efficiency. So the following studies of the article will focus on this sample.

It has been proved that heat treatment is a good way to improve the electrochemical properties of the $Na_2S_2O_8$ processed material, and the phase transformation from layered to spinel undoubtedly plays an important role in the enhanced performances. Therefore, further researches were done to study the influence of different annealing temperatures.

The power XRD was carried out to examine the structural changes in N-40 sample after being annealed at 300, 400, 500 and 600 °C. Fig. 3a shows that all the samples have a well-defined
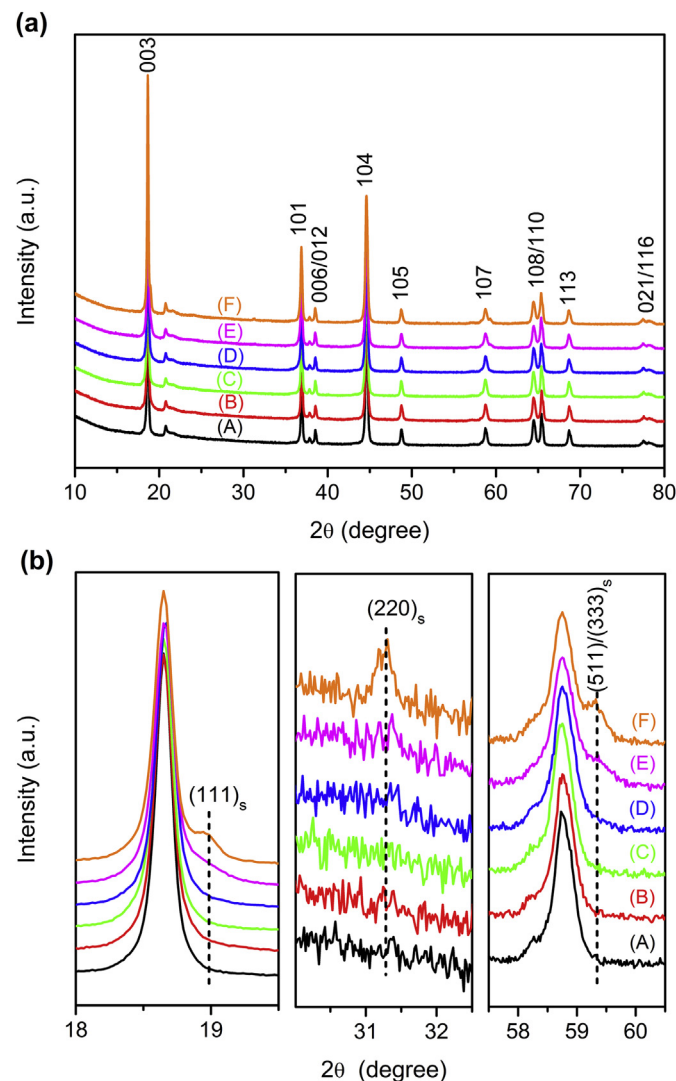
capacity is still lower than the pristine sample. Therefore, although the treatment with $Na_2S_2O_8$ aqueous solution successfully extracts Li^+ from the material, it increases the polarization of the active material due to surface damage at the same time.

Fig. 2b shows the initial charge/discharge curves of the 300 °C annealed samples cycling between 2.0 and 4.6 V at 0.1 C. Surprisingly, the initial coulombic efficiency increases from 85.4% of the pristine sample to 92.4, 93.2 and 95.6% of N-30, N-40 and N-50 samples. The corresponding initial discharge capacity also increases from 257 to 282, 285 and 284 mAh g^{-1}. Moreover, when being charged to 4.8 V, the N-40 sample can deliver a discharge capacity of 310 mAh g^{-1}, as shown in the Supporting information (Fig. S2). The superior performances imply that the broken structures of the $Na_2S_2O_8$ treated samples can be mended during heat treatment. And the slight spinel voltage platforms around 2.8 V in the profiles of all the annealed samples indicate that a small amount of spinel phases have been generated, which are believed to be helpful to improve the electrochemical properties [30–32]. In addition, the initial coulombic efficiency increases regularly with the increasing concentration of $Na_2S_2O_8$. This result can be further proved in Supplementary Fig. S3. It shows the initial charging/discharging cycle curves of the pristine sample and the 300 °C annealed samples treated with 3.5 wt.% (N-3.5), 14 wt.% (N-14), 21 wt.% (N-21),

Fig. 3. Powder XRD patterns of the pristine sample (A); the unannealed N-40 sample (B) and the N-40 sample annealed at 300 °C (C); 400 °C (D); 500 °C (E); 600 °C (F). The entire range from 10 to 80° 2θ is shown in (a) and partial enlarged view is shown in (b).

trigonal α-NaFeO$_2$ or rhombohedral α-NaFeO$_2$ layered structure with a space group R-$3m$. LiMn$_6$ super lattice reflections in the transition metal layer can be clearly seen around 20–25° 2θ, corresponding to the monoclinic Li$_2$MnO$_3$ phase (space group: $C2/m$) [12,15,20]. Only a slight difference can be found between the pristine and the treated samples, suggesting that most of the bulk structure of the material does not change during processing. Fig. 3b displays a partial enlarged view of Fig. 3a. The spinel peaks of (111)$_s$ in the left panel and (511)$_s$ in the right panel appear in the annealed samples demonstrate the formation of disordered spinel structure (LiM$_2$O$_4$-type spinel, M stands for Mn, Ni and Co). And the growing intensity of the two peaks suggests that the spinel amount increases with the rising temperature. Interestingly, the spinel structure undergoes an inner phase transition at high annealing temperature, which is supported by the appearance of (220)$_s$ peak in the middle panel. This peak can be attributed to the transition metals (Ni, Co and Mn) migrate from the 16d octahedral sites to the 8a tetrahedral sites in $Fd3m$ symmetry (Wyckoff positions) [33]. In order to distinguish it from the LiM$_2$O$_4$-type spinel structure, we refer to this kind of structure as M$_3$O$_4$-type spinel (M stands for Mn, Ni and Co). Kyung-Wan Nam et al. [33] observed several structural transformations including R-$3m$ (layered) to $Fd3m$ (LiM$_2$O$_4$-type spinel) to $Fd3m$ (M$_3$O$_4$-type spinel) when calcined the overcharged Li$_x$Ni$_{1/3}$Co$_{1/3}$Mn$_{1/3}$O$_2$ ($x = 0.33$) cathode material from 25 to 600 °C. For the similar structure between Li$_{1.143}$Mn$_{0.544}$Ni$_{0.136}$Co$_{0.136}$O$_2$ and LiNi$_{1/3}$Co$_{1/3}$Mn$_{1/3}$O$_2$, it is reasonable to deduce that, in our case, the same structural transformations take place during the annealing temperature rising from 300 to 600 °C. After Li$^+$ being extracted in Na$_2$S$_2$O$_8$ aqueous solution, the state of the material surface, in a way, is similar to overcharge. When the treated material is annealed at 300 °C, a structural transformation from layered structure to LiM$_2$O$_4$-type spinel structure comes about first. Further raising the annealing temperature to 600 °C, part of the LiM$_2$O$_4$-type spinel structure transforms to the M$_3$O$_4$-type spinel structure.

As XRD is a bulk-averaging technique, a small amount of spinel phase generates at the material surface, which can be observed in the electrochemical curves in Fig. 2b, is failed to be detected accurately. Meanwhile, the low X-ray intensity is also a problem. For TEM is a technique which can provide high-spatial resolution data on local structure, it was employed to investigate the atomic changes in N-40 sample after heat treatment. Fig. 4 displays the HRTEM images of the surface areas after being annealed at 300 °C and 400 °C. Panel a presents clear coexistence of layered and spinel domains in one particle (300 °C annealed sample), which can be certified by the Fast Fourier Transformation (FFT) image as shown in Panel b. The zone axises applied for this image are [0001]$_R$, [103]$_M$ and [−111]$_S$. And the corresponding simulated diffraction pattern is shown in Panel g, resulting from the superposition of the patterns from Panel c to Panel f. Panel c and Panel d are the conventional diffraction patterns of Li-rich layered oxides [19,34]. The former represents LiMO$_2$-like domains along [0001] zone axis,
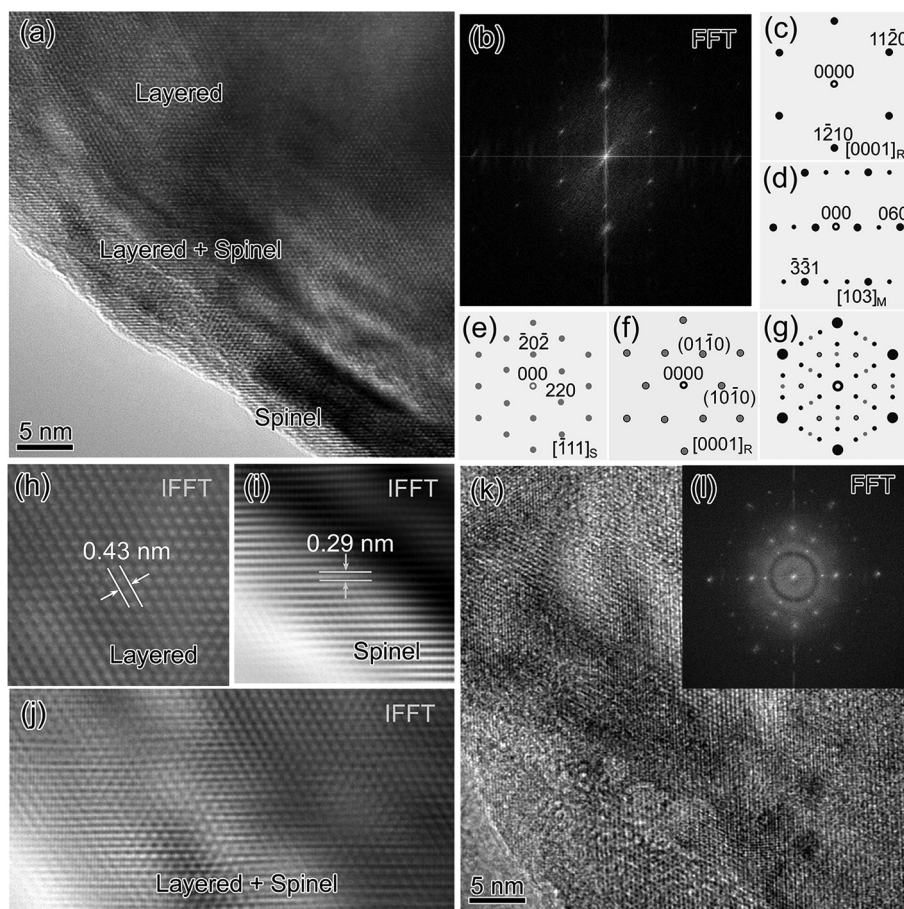

Fig. 4. HRTEM identification of (a) 300 °C and (k) 400 °C annealed samples. (b) The fast flourier transformation (FFT) to Panel a. (c) Simulated SAED pattern of rhombohedral phase along [0001] zone axis. (d) Simulated SAED pattern of monoclinic phase along [103] zone axis. (e) Simulated SAED pattern of cubic spinel phase along [−111] zone axis. (f) Simulated SAED pattern of forbidden {10−10} reflection along [0001] zone axis. (g) The superimposition of the above simulated SAED patterns. (h), (i) and (j) are inverse FFT (IFFT) images providing lattice fringes for layered and spinel phases. (l) The FFT to Panel k.

which refers to the fundamental reflections. The later stands for the Li_2MnO_3-like domains along [103] zone axis, which corresponds to the super-reflections along three equivalent {11−20} poles. The FFT image can be designated as the superposition of a rhombohedral $LiMO_2$ pattern and three monoclinic Li_2MnO_3 patterns rotated 120° about the [0001] zone axis [34]. In addition, the extra spots are associated with the spinel donations along [−111] zone axis in Panel e as well as the forbidden reflections {10−10} along [0001] zone axis in Panel f. The appearance of the forbidden reflections suggests that the rhombohedral phase is disturbed in some crystals with staking faults or dislocation [35]. The inverse FFT (IFFT) image in Panel i exhibits the lattice spacing of 0.29 nm, which is well consistent with the (220) plane along with [−111] zone axis from cubic spinel phase. Note that this spinel phase focuses on the particle surface, forming a spinel layer with about 5 nm thickness. It is reasonable to deduce that these surface spinels play a critical role in fast intercalation/extraction of Li^+ and electrons during electrochemical cycles. In Panel h, the distance between two lattice fringes was calculated to be 0.43 nm, which is identified with (020) plane of the monoclinic phase. It is separated by the layered-spinel intermediate zone in Panel j, where two kinds of lattice fringes are coexistent, implies that the phase transition from layered to spinel happens here. Panel k presents the 400 °C annealed sample with its FFT image as an inset. The spinel spots in the FFT image becomes more obvious than 300 °C annealed sample, demonstrates that more layered phase has transformed to spinel phase, and achieves good agreement with the result observed above. But we also notes that the structural regularity of the particle surface has deteriorated. As the process of structural transformation from LiM_2O_4-type spinel to M_3O_4-type spinel is accompanied by the release of oxygen, which will influence the surface structural regularity of the material, we can deduce that the inner structural evolution of the spinel structure starts below 400 °C.

X-ray photoelectron spectroscopy (XPS) analyses were carried out to further investigate the reaction mechanisms of the treatments of $Na_2S_2O_8$ aqueous solution and annealing. Fig. 5 shows the Mn 2p, Co 2p, Ni 2p and O 1s spectra of N-40 sample before and after heat treatment. For the spectra with respect to Mn 2p, Co 2p and Ni 2p orbital, the binding energies remain unchanged over the treatments, indicating that Mn, Co and Ni do not participate in

the redox processes. Turning to the O1s spectra in Fig. 5d, two peaks characteristic of O^{2-} anions belonging to the crystalline network (529.5 eV peak) and weakly absorbed surface species (531.0 eV peak) are clearly visible in the pristine sample [36]. The latter is also responsible for the weak signal at about 533.5 eV. Surprisingly, after the material being treated with 40 wt.% $Na_2S_2O_8$, two new peaks appear at 530.1 eV and 531.9 eV. It is important to note that the sum of peak area percentages at 529.5 eV and 530.1 eV here is equal to the peak area percentage at 529.5 eV in the pristine sample, and the same is true of the relationship between the sum of peak area percentages at 531 eV and 531.9 eV here and the peak area percentage at 531 eV in the pristine sample. The component at 530.1 eV can be attributed to oxidation of the lattice oxygen to the formal O_2^{2-} specie. Similar transformation has been reported by Sathiya et al. [37,38] which confirms the possibility of the formal O_2^{2-} species existing at the surface of Li-rich layered oxides when they are in charging state. The other component at 531.9 eV is due to the oxidation products of the surface species after being treated with $Na_2S_2O_8$ aqueous solution. However, after being annealed at 300 °C, both of the two peaks disappear and the shape of the O1s spectrum converses back to the pristine. No more obvious changes occur at higher temperatures. Since the poor thermal stability of the new generated components, it is reasonable to deduce that they have decomposed during the annealing at 300 °C. Based on the above observations, we can conclude the reaction processes as follows: When being treated with $Na_2S_2O_8$ aqueous solution, Li^+ is extracted from the material and the corresponding lattice oxygen is oxidized to the formal O_2^{2-} species. During the annealing at 300 °C, the generated formal O_2^{2-} species transforms to O^{2-} anions and O_2 through a disproportionation reaction due to its unstable structure. Then O_2 releases from the particle surface, causing some changes (such as oxygen vacancies increased, lattice staggered and cations rearranged et al.) of the crystal structure which induce the formation of spinel phase. For the valence states of Mn, Co and Ni do not change obviously during all the treatments, it is reasonable to deduce that O_2 mainly releases from the Li_2MO_3 (M stands for Mn, trace doped Ni and Co) region, where the transition metals are in the tetravalent state, and difficult to be further oxidized. The ideal reaction formulae can be denoted as below:
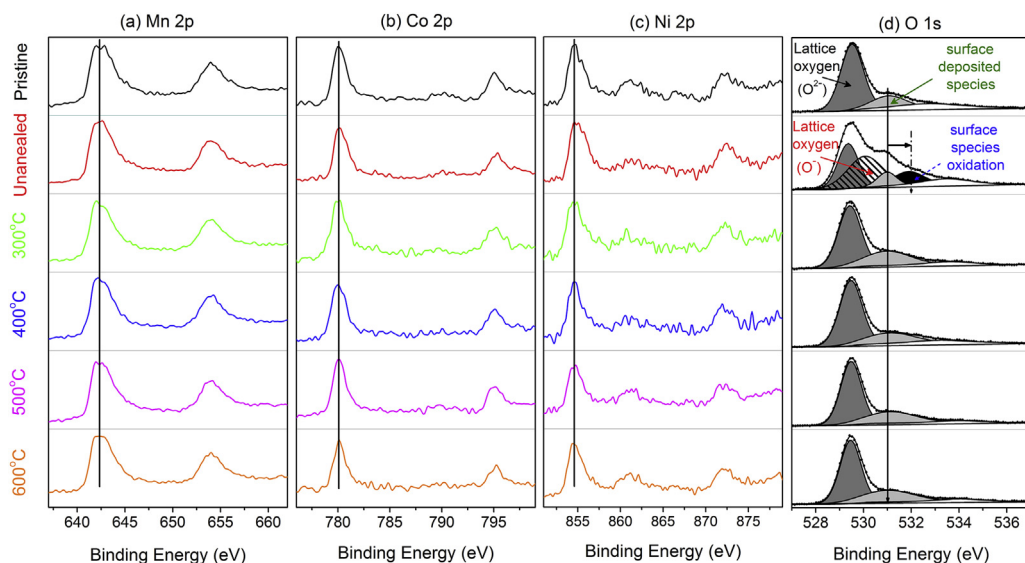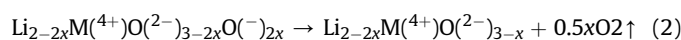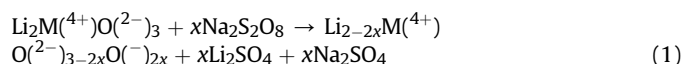

Fig. 5. XPS spectra of (a) Mn 2p, (b) Co 2p, (c) Ni 2p and (d) O 1s. From top to bottom, the spectra were collected from the pristine sample, the unannealed N-40 sample and the N-40 sample annealed at 300, 400, 500 and 600 °C.

$$Li_2M(^{4+})O(^{2-})_3 + xNa_2S_2O_8 \rightarrow Li_{2-2x}M(^{4+})$$
$$O(^{2-})_{3-2x}O(^-)_{2x} + xLi_2SO_4 + xNa_2SO_4 \qquad (1)$$

$$Li_{2-2x}M(^{4+})O(^{2-})_{3-2x}O(^-)_{2x} \rightarrow Li_{2-2x}M(^{4+})O(^{2-})_{3-x} + 0.5xO2\uparrow \quad (2)$$

The first (Equation (1)) is associated with the generation of the formal O_2^{2-} species, resulting from the chemical de-lithiation from the Li_2MO_3 region. The second (Equation (2)), with the release of oxygen, corresponds to the decomposition of the formal O_2^{2-} species during the annealing at 300 °C.

Fig. 6a shows the first charge/discharge curves of the pristine sample and N-40 sample before and after heat treatments (300, 400, 500 and 600 °C). With the increasing of annealing temperature, the spinel voltage platform becomes more and more obviously, indicating the amount of spinel phase is proportional to the annealing temperature. It is well consistent with the results of XRD tests. In addition, the spinel voltage platform also undergoes a descending process from 2.8 to 2.6 V, which may be due to the structural evolution from LiM_2O_4-type spinel structure to M_3O_4-type spinel structure. Unlike the LiM_2O_4-type spinel structure with three-dimensional lithium ion diffusion channels, the M_3O_4-type spinel structure, with both tetrahedral- and octahedral-sites are occupied by the transition metal atoms, shows very low lithium ion conductivity. Therefore, the initial discharge capacity decreases gradually with the annealing temperature rising from 300 to 600 °C. The corresponding initial coulombic efficiency also decreases from 93.2% (300 °C) to 89.7% (600 °C). Fig. 6b compares the rate capability of the pristine sample and the 300 °C annealed N-40 sample. They were tested at incremental C rates of 0.1, 0.2, 0.5 and 1 C charge/discharge rate. The 300 °C annealed sample manifests its good rate performance. Especially at 1 C charge/discharge rate, it

can exhibit a maximal capacity of 217 mAh g^{-1}, much higher than that of the pristine sample (190 mAh g^{-1}). Fig. 6c shows that the pristine sample delivers a maximal capacity of 261 mAh g^{-1} with retention of 92.2% after 50 cycles. For the N-40 sample without annealing treatment, the capacity presents a significant decrease, which goes through a slow activated process from lower than 100 mAh g^{-1} to about 240 mAh g^{-1} in the initial 20 cycles. However, after being annealed at 300 °C, it can deliver a maximal capacity of 285 mAh g^{-1} with retention of 92.9% after 50 cycles. From the above results, we can conclude that the surface spinel layer generated after $Na_2S_2O_8$ aqueous solution and annealing treatments is beneficial to enhance the electrochemical performance of the material.

Electrochemical impedance spectra (EIS) were measured to obtain a better understanding of the impact of the structural transformation on the electrochemical properties. Fig. 7a presents the room-temperature Nyquist plots at the first time charging state of 4.6 V. An equivalent circuit model, as shown in Fig. 7b, was applied to fit the raw data from EIS measurements to obtain the accurate value of the impedances. All of the plots show a small interrupt and a semicircle in the high frequency range, a semicircle in the intermediate frequency range and a sloped straight line in the low frequency range. The small interrupt in the high frequency range is related to the electrolyte impedance (R_e). The semicircle in the high frequency range represents the impedance of Li$^+$ diffusion in the surface layer (SEI film) of the composite cathode (R_s). The other semicircle in the intermediate frequency range refers to the charge transfer impedance in the electrode/electrolyte interface (R_{ct}). And the sloped straight line in the low frequency range stands for the Warburg impedance (Z_w) for describing Li$^+$ diffusion in the bulk region of the material. In our case, both R_s and R_{ct} reflect
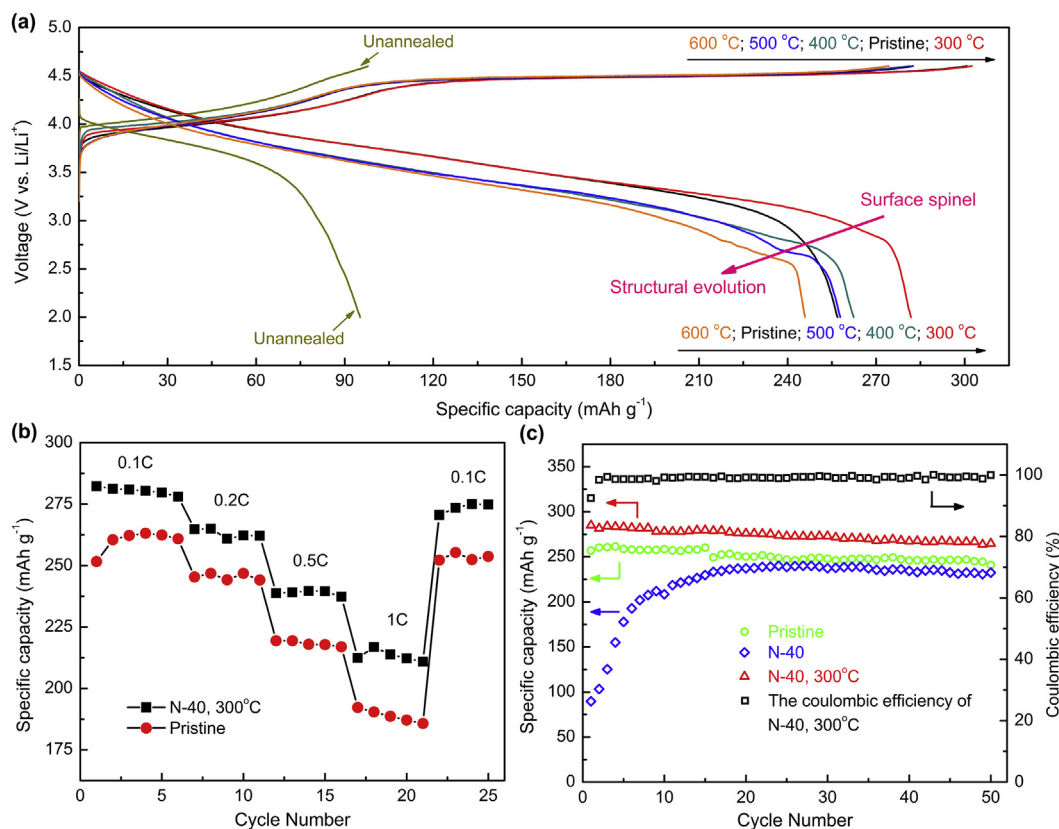

Fig. 6. (a) The initial charge/discharge curves of the pristine sample, the unannealed N-40 sample and the N-40 sample annealed at 300, 400, 500 and 600 °C. (b) Rate capability of the pristine sample and the 300 °C annealed N-40 sample. (c) Cycle performance of the pristine sample, the unannealed N-40 sample and the 300 °C annealed N-40 sample (its coulombic efficiencies are expressed by the black squares). (a) and (c) were cycled between 2.0 and 4.6 V at 0.1 C rate where 1 C stands for 250 mA g^{-1}.
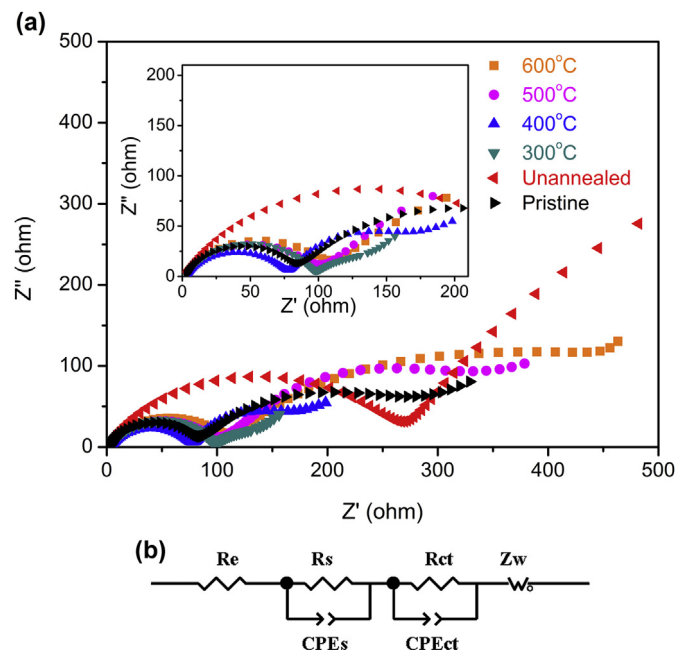
(a)

(b)

Fig. 7. (a) EIS plots of the pristine sample, the unannealed N-40 sample and the N-40 sample annealed at 300, 400, 500 and 600 °C. (b) The equivalent circuit used for NLLS-fitting of the experimental data.

surface features. As shown in Fig. 7a, they undergo a similar changing process. The detailed impedance parameters of all the samples are shown in the Supporting Information (Table S1). In particular, the R_{ct} of the pristine sample is 179.6 Ω, but surprisingly, it rises to 1292 Ω after being treated with 40 wt.% $Na_2S_2O_8$. More surprisingly, it decreases to 38.5 Ω after the annealing at 300 °C. Then it increases gradually with the increase of the annealing temperature, and the 600 °C annealed sample reaches 326.4 Ω, has exceeded the value of the pristine sample. Obviously, the above changing process of the impedances is well consistent with the surface structural transformation of the material from layered to LiM_2O_4-type spinel to M_3O_4-type spinel.

4. Conclusion

The surface structure of the Li-rich layered $Li_{1.143}Mn_{0.544}Ni_{0.136}Co_{0.136}O_2$ cathode material was successfully transformed from layered to spinel through the treatments of $Na_2S_2O_8$ aqueous solution and annealing. Benefited by the formed surface spinel layer, the surface structure of the modified material becomes more stable during the process of the electrochemical activation, in addition to reduce the internal resistance. It is found that the treatments by 40 wt.% $Na_2S_2O_8$ and 300 °C annealing can improve the initial discharge capacity most from 257 to 285 mAh g^{-1} (corresponding to the initial coulombic efficiency increases from 85.4% to 93.2%), in addition to enhance rate performance. The mechanism of spinel formation has been detailed studied by ICP, HRTEM, SEM, XRD, XPS, EIS and electrochemical measurements. The results indicate that Li$^+$ in the Li_2MO_3 region can be successfully extracted by $Na_2S_2O_8$ aqueous solution and the corresponding lattice oxygen is oxidized to formal O_2^{2-} species and retained in the Li_2MO_3 region, other than being oxidized to O_2 and releasing from particle surface. After the treated materials being annealed at elevated temperatures (300, 400, 500 and 600 °C), the generated formal O_2^{2-} species disappears, resulting in a spinel layer forms at the particle surface. For the poor thermal stability of the formal O_2^{2-} species, it is reasonable to deduce that it turns to O_2 and releases from the

particle surface during annealing treatment. Meanwhile, the increased oxygen vacancies induce cationic rearrangement and lead to the structural transformation from layered (R-$3m$ or $C2/m$) to spinel ($Fd3m$). Besides, the spinel phase undergoes an inner structural evolution from LiM_2O_4-type to M_3O_4-type at high annealing temperature. It reveals the reason why the electrochemical performance deteriorates gradually with the annealing temperature increasing from 300 to 600 °C. To the best of our knowledge, this is the first study to report such a conversion in Li-rich layered cathode materials.

In conclusion, the method studied in this article has been proved to effectively enhance the material's initial coulombic efficiency as well as the charge/discharge capability. Compared with the surface coating, it achieves the similar improvements with more simple processing technology [23–29]. We believe that if the process of chemical Li$^+$ de-intercalation can be more facile, the electrochemical performance obtained will be better, especially in long-term cyclic stability. It may provide a new insight on surface modification of Li-rich layered cathode materials for the next generation of lithium-ion batteries.

Appendix A. Supplementary data

Supplementary data related to this article can be found at http://dx.doi.org/10.1016/j.jpowsour.2014.06.106.

References

[1] M. Armand, J.M. Tarascon, Nature 451 (2008) 652–657.
[2] Y.-M. Chiang, Science 330 (2010) 1485–1486.
[3] B. Dunn, H. Kamath, J.M. Tarascon, Science 334 (2011) 928–935.
[4] J.M. Tarascon, M. Armand, Nature 414 (2001) 359–367.
[5] N.-S. Choi, Z. Chen, S.A. Freunberger, X. Ji, Y.-K. Sun, K. Amine, G. Yushin, L.F. Nazar, J. Cho, P.G. Bruce, Angew. Chem. Int. Ed. 51 (2012) 9994–10024.
[6] K. Mizushima, P.C. Jones, P.J. Wiseman, J.B. Goodenough, Mater. Res. Bull. 15 (1980) 783–789.
[7] D. Caurant, N. Baffier, B. Garcia, J.P. Pereira-Ramos, Solid State Ionics 91 (1996) 45–54.
[8] T. Ohzuku, Y. Makimura, Chem. Lett. 30 (2001) 642–643.
[9] J.M. Tarascon, E. Wang, F.K. Shokoohi, J. Electrochem. Soc. 138 (1991) 2859–2864.
[10] A.K. Padh, K.S. Nanjundoswamy, J.B. Goodenough, J. Electrochem. Soc. 144 (1997) 1188–1194.
[11] M.M. Thackeray, C. Wolverton, E.D. Isaacs, Energy Environ. Sci. 5 (2012) 7854–7863.
[12] Z.H. Lu, D.D. MacNeil, J.R. Dahn, Electrochem. Solid-State Lett. 4 (2001) A191–A194.
[13] J.S. Kim, C.S. Johnson, J.T. Vaughey, M.M. Thackeray, S.A. Hackney, W. Yoon, C.P. Grey, Chem. Mater. 16 (2004) 1996–2006.
[14] M.M. Thackeray, S.H. Kang, C.S. Johnson, J.T. Vaughey, S.A. Hackney, Electrochem. Commun. 8 (2006) 1531–1538.
[15] M.M. Thackeray, S.H. Kang, C.S. Johnson, J.T. Vaughey, R. Benedeka, S.A. Hackney, J. Mater. Chem. 17 (2007) 3112–3125.
[16] C.S. Johnson, C.N. Li, C. Lefief, J.T. Vaughey, M.M. Thackeray, Chem. Mater. 20 (2008) 6095–6106.
[17] N. Yabuuchi, K. Yoshii, S.T. Myung, I. Nakai, S. Komaba, J. Am. Chem. Soc. 133 (2011) 4404–4419.
[18] J. Bareno, C.H. Lei, J.G. Wen, S.-H. Kang, I. Petrov, D.P. Abraham, Adv. Mater. 22 (2010) 1122–1127.
[19] H. Yu, R. Ishikawa, Y.-G. So, N. Shibata, T. Kudo, H. Zhou, Y. Ikuhara, Angew. Chem. Int. Ed. 52 (2013) 5969–5973.
[20] A.R. Armstrong, M. Holzapfel, P. Novak, C.S. Johnson, S.H. Kang, M.M. Thackeray, P.G. Bruce, J. Am. Chem. Soc. 128 (2006) 8694–8698.

[21] J. Hong, H.-D. Lim, M. Lee, S.-W. Kim, H. Kim, S.-T. Oh, G.-C. Chung, K. Kang, Chem. Mater. 24 (2012) 2692–2697.
[22] A. Ito, D. Li, Y. Sato, M. Arao, M. Watanabe, M. Hatano, H. Horie, Y. Ohsawa, J. Power Sources 195 (2010) 567–573.
[23] Y. Wu, A. Manthiram, Solid State Ionics 180 (2009) 50–56.
[24] Q.Y. Wang, J. Liu, A. Vadivel Murugan, A. Manthiram, J. Mater. Chem. 19 (2009) 4965–4972.
[25] M.-S. Park, J.-W. Lee, W. Choi, D. Im, S.-G. Doo, K.-S. Park, J. Mater. Chem. 20 (2010) 7208–7213.
[26] F. Wu, N. Li, Y. Su, H. Lu, L. Zhang, R. An, Z. Wang, L. Bao, S. Chen, J. Mater. Chem. 22 (2012) 1489–1497.
[27] Y.-K. Sun, M.-J. Lee, C.S. Yoon, J. Hassoun, K. Amine, B. Scrosati, Adv. Mater. 24 (2012) 1192–1196.
[28] S.H. Kang, M.M. Thackeray, Electrochem. Commun. 11 (2009) 748–751.
[29] Q.Q. Qiao, H.Z. Zhang, G.R. Li, S.H. Ye, C.W. Wang, X.P. Gao, J. Mater. Chem. A 1 (2013) 5262–5268.
[30] F. Wu, N. Li, Y. Su, H. Shou, L. Bao, W. Yang, L. Zhang, R. An, S. Chen, Adv. Mater. 25 (2013) 3722–3726.
[31] B. Song, H. Liu, Z. Liu, P. Xiao, M.O. Lai, L. Lu, Sci. Rep. 3 (2013).
[32] J. Zheng, S. Den, Z. Shi, H. Xu, H. Xu, Y. Deng, Z. Zhang, G. Chen, J. Power Sources 221 (2013) 108–113.
[33] K.-W. Nam, S.-M. Bak, E. Hu, X. Yu, Y. Zhou, X. Wang, L. Wu, Y. Zhu, K.-Y. Chung, X.-Q. Yang, Adv. Funct. Mater. 23 (2013) 1047–1063.
[34] D. Mohanty, S. Kalnaus, R. Meisner, K.J. Rhodes, J. Li, E.A. Payzant, D.L. Wood III, C. Daniel, J. Power Sources 229 (2013) 239–248.
[35] J. Bareno, M. Balasubramanian, S.H. Kang, J.G. Wen, C.H. Lei, S.V. Pol, I. Petrov, D.P. Abraham, Chem. Mater. 23 (2011) 2039–2050.
[36] J.C. Dupin, D. Gonbeau, P. Vinatier, A. Levasseur, Phys. Chem. Chem. Phys. 2 (2000) 1319–1324.
[37] M. Sathiya, K. Ramesha, G. Rousse, D. Foix, D. Gonbeau, A.S. Prakash, M.L. Doublet, K. Hemalatha, J.-M. Tarascon, Chem. Mater. 25 (2013) 1121–1131.
[38] M. Sathiya, G. Rousse, K. Ramesha, C.P. Laisa, H. Vezin, M.-L. Doublet, D. Foix, D. Gonbeau, W. Walker, A.S. Prakash, M. Ben Hassine, L. Dupont, J.-M. Tarascon, Nat. Mater. 12 (2013) 827–835.